Journal of Alloys and Compounds 509 (2011) 9171–9177

Contents lists available at ScienceDirect

Journal of Alloys and Compounds

journal homepage: www.elsevier.com/locate/jallcom

Enhanced NO_2 sensing characteristics of Pd-functionalized networked In_2O_3 nanowires

Sang Sub Kim [a], Jae Young Park [a], Sun-Woo Choi [a], Han Gil Na [b], Ju Chan Yang [b], Hyoun Woo Kim [b,*]

[a] Division of Materials Science and Engineering, Inha University, Incheon 402-751, Republic of Korea
[b] Division of Materials Science and Engineering, Hanyang University, Seoul 133-791, Republic of Korea

ARTICLE INFO

Article history:
Received 30 December 2010
Received in revised form 23 June 2011
Accepted 23 June 2011
Available online 30 June 2011

Keywords:
Indium/indium compounds
Nanomaterials
Sensors
Palladium/palladium compounds

ABSTRACT

In this work, we fabricated Pd-functionalized networked In_2O_3 nanowires. For the Pd-functionalization, In_2O_3–Pd core–shell nanowires were synthesized by depositing Pd layers using a sputtering method on bare In_2O_3 nanowires. The continuous Pd shell layers were transformed into islands of cubic Pd/PdO phase by thermal heating. We compared the NO_2 sensing characteristics of the sensors fabricated from Pd-functionalized and bare In_2O_3 nanowires, respectively. The results demonstrated that Pd functionalization greatly improves sensitivity and response time in In_2O_3 nanowire-based gas sensors. The improvement of sensing properties is likely caused by not only the enhanced adsorption or dissociation of NO_2, but also the associated spillover effects, which are both caused by the Pd-functionalization.

1. Introduction

Indium oxide (In_2O_3), an important n-type semiconductor, has been extensively studied due to its advantageous features, such as significant large energy band gap (3.5–3.75 eV) [1], high electrical conductivity [2], excellent luminescence [3,4], and high optical transparency [5]. Accordingly, it has a wide range of practical applications, including optoelectronic devices [6], solar cells [7], field effect transistors [8], electric-double-layer transistors [9], Fabry–Perot resonators [10], thin-film transistors [11], bio sensors, and gas sensors. In_2O_3 has attracted much attention for its ability to sense both oxidizing and reducing gases, including O_2 [12], O_3 [13,14], nitric oxides [15], CO [16,17], H_2S [18], H_2 [16,17], and noxious volatile organic compounds [19].

The detection and control of toxic gases such as nitrogen oxide (NO_x) by sensitive and reversible sensors has become a crucial aspect of environmental consciousness, because these gases have destructive effects on the human respiratory system [20]. NO_2 is one of the most harmful gases, as it is emitted from combustion of the exhaust of automobile engines, home heaters, furnaces, plants, etc. Accordingly, it is necessary to develop sensors with sufficient sensitivity and quick response time to detect NO_2 at low concentrations, such as a few ppm, in the ambient [21]. Previous reports demonstrated that In_2O_3 thin-film sensors are sensitive to low concentrations of NO_2 gas in air [14,22–25].

On the other hand, nanoscale materials in the form of nanowires, nanotubes, and nanoribbons have great potential for use as highly sensitive chemical sensors [26,27]. Their extremely high surface-to-volume ratios and single crystallinity in regard to one-dimensional (1D) nanostructures may explain why the sensors are much more sensitive than those made from conventional materials. In single-crystalline sensors, the faces exposed to gaseous environments are always the same and almost all of the adsorbed species are active in generating a surface depletion layer [28,29], whereas only a small fraction of the adsorbed species near the grain boundaries are active in modifying electrical transport properties in polycrystalline devices. Several researchers have reported the NO_2 gas sensing properties of In_2O_3 nanowires [30–32].

In addition, the use of metallic catalysts can functionalize the surface of nanomaterials by means of catalytic effects. Although the addition of noble metals to 1D nanostructures of In_2O_3 is known to enhance gas sensitivity, to the best of our knowledge, no work has been reported on Pd-functionalized In_2O_3 nanowires, in terms of NO_2 sensitivity. The ethanol sensing properties of Pd-doped In_2O_3 nanowires have been previously researched [33]. Moreover, the effect of Pd sensitization on the H_2S sensing properties of La-doped In_2O_3 powders was examined [34]. The As-doping in In_2O_3 nanoparticles were effective in obtaining highly sensitive and selective alcohol sensors [35].

In the present work, we fabricated networked In_2O_3 nanowires for use in gas sensors and subsequently functionalized their surfaces with Pd by using a conventional sputtering and subsequent heat treatment process. We compared the sensing characteristics for Pd-functionalized In_2O_3 nanowires and bare ones with respect

* Corresponding author.
E-mail address: hyounwoo@hanyang.ac.kr (H.W. Kim).

0925-8388/$ – see front matter © 2011 Elsevier B.V. All rights reserved.
doi:10.1016/j.jallcom.2011.06.104

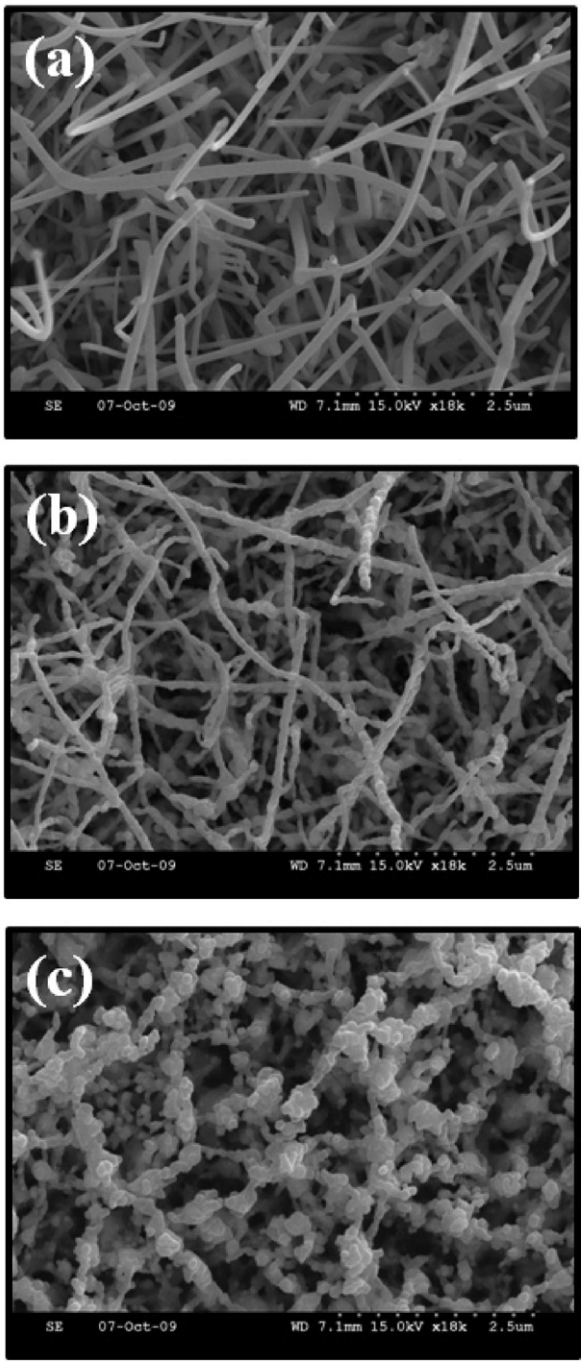

Fig. 1. SEM images of (a) as-deposited, (b) 700 °C-annealed, and (c) 900 °C-annealed core–shell nanowires.

to NO_2 gas. This study will not only explore the use of fabricated networked In_2O_3 nanowires for the detection of low-concentration NO_2 gas, but also contribute to the development of a simple and efficient method of Pd-functionalization of the nanowire surface for general gas sensing.

2. Experimental details

The experimental apparatus used to fabricate the core In_2O_3 nanowires was a tube furnace, in which the source material and Au (approximate thickness = 3 nm)-coated Si substrate were placed on the lower and upper holders, respectively, in the center of a quartz tube inserted into a vertical furnace. As a source material, a mixture of In and Mg powders with a weight ratio of 1:1 was employed. In preliminary study, no thin nanowire was obtained by conducting the same experiments using the pure Mg powders. It is surmised that Mg lowers the melting point of the In–Mg alloy. Accordingly, the source materials are more likely to exist as a liquid, which is favorable for the vapor–liquid–solid (VLS) process. A mixture of Ar and O_2 gases, with a percentage of the O_2 partial pressure of 3%, was flowed for 1 h with a constant total flow rate of 2 standard liters per min (slm) at 800 °C. The existence of an Au-related tip suggested that the nanowires were grown via a vapor–liquid–solid (VLS) process.

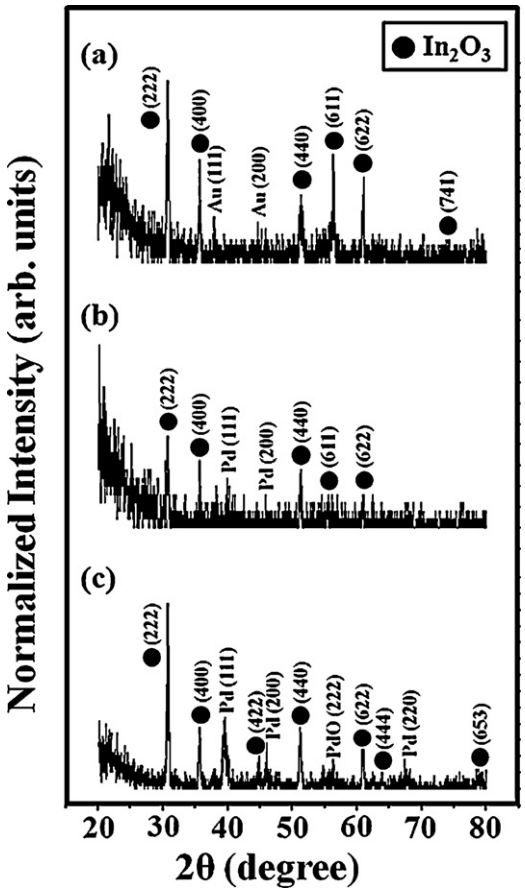

Fig. 2. XRD spectra of (a) core nanowires, (b) as-deposited, and (c) 700 °C-annealed core–shell nanowires.

Following this, the substrate was transferred to a turbo sputter coater (Emitech K575X, Emitech Ltd., Ashford, Kent, UK). By using a circular Pd target at room temperature, the sputter time was set to 2 min in high-purity (99.999%) argon (Ar) ambient. During the sputtering process, the DC current was maintained at 65 mA. Subsequently, the In_2O_3/Pd core–shell nanowires were annealed for 30 min in Ar ambient, at temperatures in the range of 500–900 °C.

The samples were examined by X-ray diffraction (XRD) using a Philips X'pert MRD diffractometer, field emission scanning electron microscope (FE-SEM; Hitachi S-4200), and transmission electron microscopy (TEM) using a Philips CM-200 TEM operating at 200 kV. The energy-dispersive X-ray (EDX) spectroscopy attached to TEM was used to investigate the composition of the product.

For the sensing measurements, Ni (~200 nm in thickness) and Au (~50 nm) double-layer electrodes were sequentially deposited via sputtering on the specimens using an interdigital electrode mask. The fabricated sensors were introduced into a vacuum chamber and electrical conductivity was measured with changing NO_2 environments at 573 K. The base pressure of the vacuum chamber, which was connected to a turbomolecular pump, was typically $\sim 5 \times 10^{-6}$ torr. Using a mass flow controller, NO_2 concentrations were adjusted while introducing NO_2 with a flow rate of 50 sccm. This configuration is the same as the experimental setup used previously by our research group [36–39].

3. Results and discussion

Fig. 1a–c shows SEM images of as-deposited, 700 °C-annealed, and 900 °C-annealed core–shell nanowires, respectively. Fig. 1a indicates that the as-deposited nanowires have a relatively smooth surface, whereas annealing induced a relatively rough surface (Fig. 1b and c). Although the surface roughness of bulk or film can be evaluated by means of a variety of technique includ-

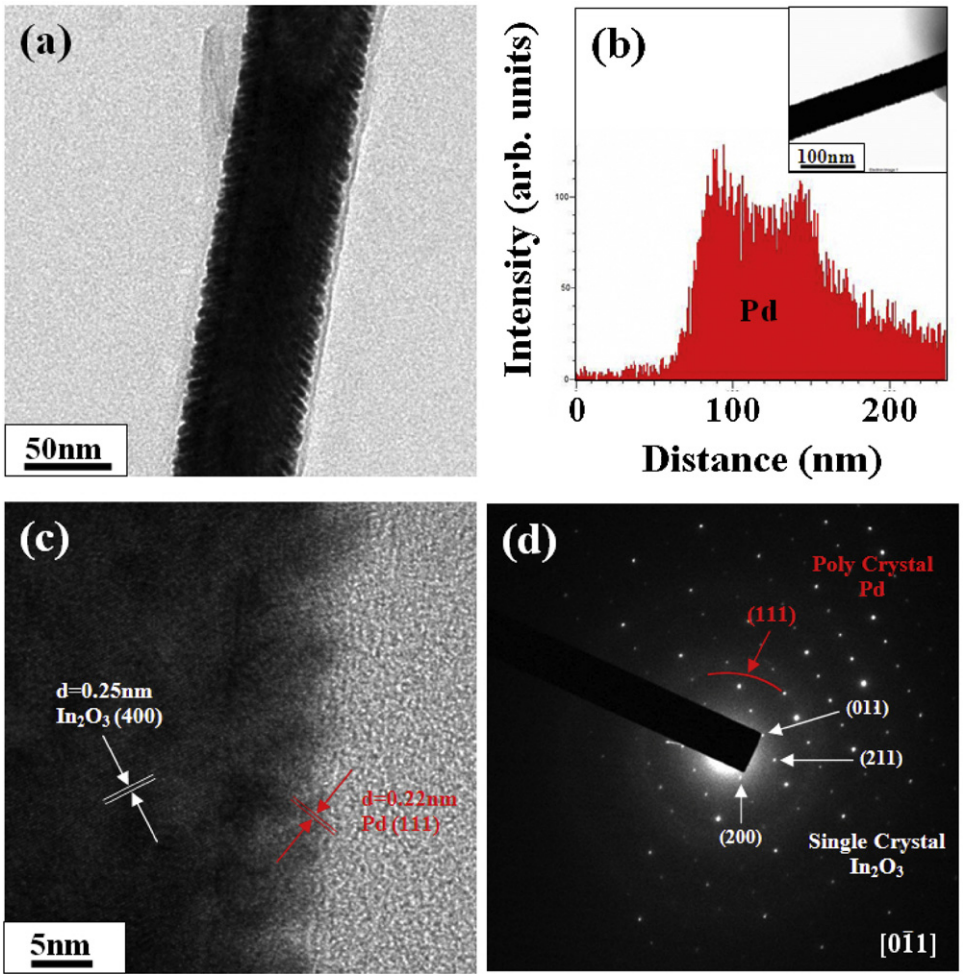

Fig. 3. (a) Low-magnification TEM image of an as-synthesized core–shell nanowire. (b) EDX line profile of Pd element across an as-synthesized core–shell nanowire (inset: corresponding TEM image). (c) Lattice-resolved TEM image and (d) SAED pattern of as-synthesized core–shell nanowires.

ing atomic force microscopy, scanning tunneling microscopy, and surface profiler, the measurement technique of surface roughness in nanowires is not set up yet. In this paper, we have used Thomas's technique, in which the vertical distance between the highest peak and the lowest valley of the surface profile, P_t [40]. The P_t of as-deposited, 700 °C-annealed, and 900 °C-annealed core–shell nanowires, respectively, were measured to be about 8, 62, and 162 nm, respectively (see the Supplementary material, S-1). It reveals that the surface roughness tends to increase as the annealing temperature increased in the range of 500–900 °C.

Fig. 2a shows an XRD pattern of the core nanowires, exhibiting both In_2O_3 and Au phases. The In_2O_3 cubic phase has a lattice parameter of $a = 10.11$ Å (JCPDS Card No. 06-0416), whereas the Au face-centered-cubic phase has a lattice parameter of $a = 4.078$ Å (JCPDS Card No. 04-0784). Fig. 2b shows an XRD pattern of the as-deposited core–shell nanowires, mainly exhibiting a cubic In_2O_3 phase. However, close examination suggests that some very weak peaks correspond to the reflection of the cubic structure of Pd with a lattice constant of $a = 3.890$ Å (JCPDS File No. 46-1043). Fig. 2c reveals that there exist (1 1 1) diffraction peaks of the cubic Pd phase. Also, it is evident that there exist a weak peak corresponding to the (2 2 2) reflection of the cubic structure of PdO with a lattice constant of $a = 5.637$ Å (JCPDS File No. 46-1211). In order to study the evolution of Pd phases by the thermal annealing, we have closely examined the XRD spectra (Supplementary materials, S-2 and S-3). It indicated that the relative XRD intensities of Pd(1 1 1) and Pd(2 0 0) peaks with respect to the In_2O_3(4 4 0) peak have been increased by the thermal annealing at 700 °C.

In order to investigate the morphological and structural changes with thermal annealing, we carried out TEM analysis. Fig. 3a shows a low-magnification TEM image of an as-synthesized core–shell nanowire, which reveals that the sputtered layer is relatively rough, resembling the saw-tooth morphology. Fig. 3b shows an EDX line profile of the Pd element across the core–shell nanowire as shown in the inset. It represents a valley-like profile, revealing that the Pd elements reside mainly in the sheath region of the core–shell nanowire. Fig. 3c shows a lattice-resolved TEM image near the outer region of the core–shell nanowire. In the core region, the spacing between lattice planes was about 0.25 nm, corresponding to spacing d_{400} of cubic In_2O_3. In the shell region, it is noteworthy that the interlayer distance was measured to be about 0.22 nm, corresponding to the {1 1 1} plane of cubic Pd. Fig. 3d shows an associated selected area electron diffraction (SAED) pattern recorded perpendicular to the rod axis, as it was indexed for the [0 $\bar{1}$ 1] zone axis of crystalline cubic In_2O_3. The well-defined SAED pattern clearly shows the diffraction spots representing {0 1 1}, {2 1 1}, and {2 0 0} lattice planes of cubic In_2O_3. In addition, the SAED pattern shows the presence of weaker ring patterns, presumably corresponding to the polycrystalline structures of cubic Pd.

On the other hand, Fig. 4a shows a low-magnification TEM image of a 700 °C-annealed core–shell nanowire. By comparing Fig. 4a with Fig. 3a, we observed that thermal annealing induced more surface roughness. In order to reveal the nature of the rough sur-

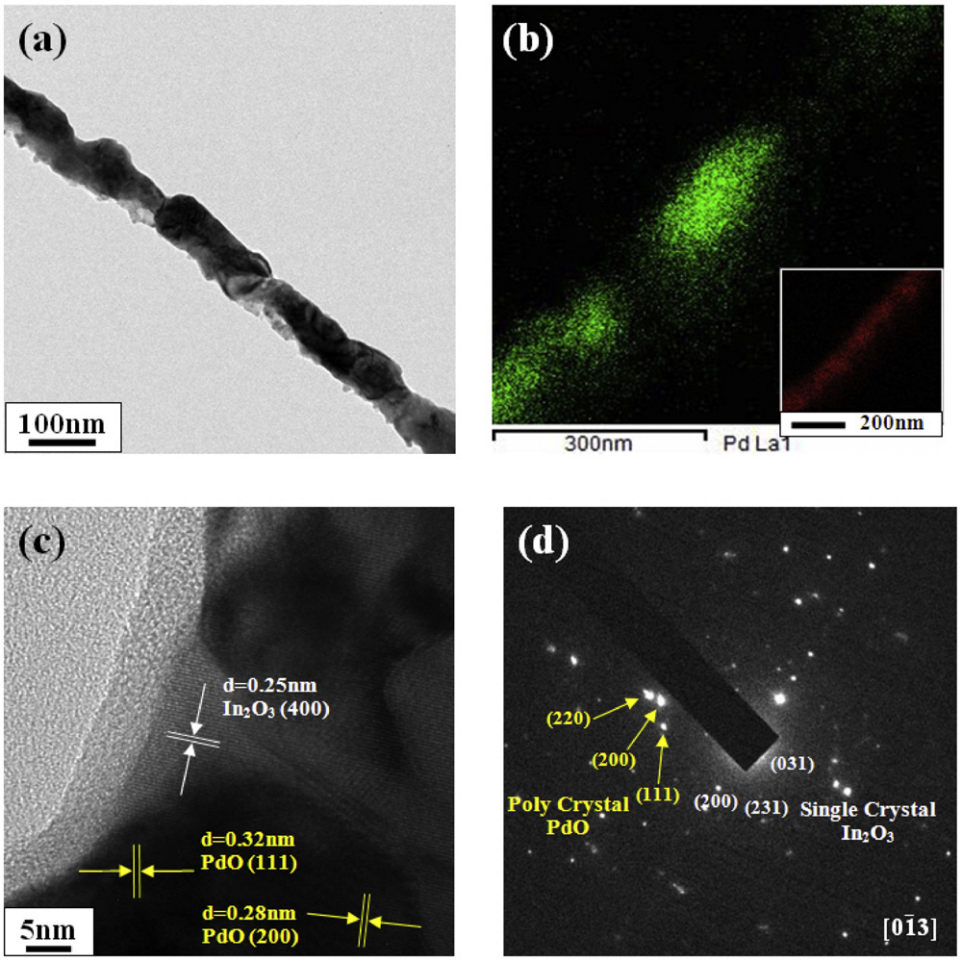

Fig. 4. (a) Low-magnification TEM image of a 700 °C-annealed core–shell nanowire. (b) EDX elemental map of Pd elements taken from a typical 700 °C-annealed core–shell nanowire (inset: corresponding EDX elemental map of In). (c) Lattice-resolved TEM image and (d) SAED pattern of 700 °C-annealed core–shell nanowires.

face, we carried out EDX analysis on the 700 °C-annealed core–shell nanowires. While Fig. 4b exhibits the elemental map of Pd, its inset shows an associated elemental map of In elements. From those elemental maps, we surmise that the sputtered Pd shell was agglomerated by thermal annealing, resulting in partial exposure of the surface of core In_2O_3 nanowires. Fig. 4c shows a lattice-resolved TEM image near the outer region of the 700 °C-annealed core–shell nanowire. In some regions, the spacing between lattice planes is about 0.25 nm, corresponding to spacing d_{400} of tetragonal In_2O_3. In other regions, it is noteworthy that the interlayer distances were measured to be about 0.32 nm and 0.28 nm, corresponding to the {1 1 1} and {2 0 0} planes of cubic PdO, with a lattice parameter of $a = 5.637$ Å (JCPDS File No. 46-1211). Fig. 4d shows an associated SAED pattern, indicating that there exist diffraction spots corresponding to the {0 1 1}, {2 1 1}, and {2 0 0} lattice planes of cubic In_2O_3. In addition, there exist spots forming the diffusion rings of {2 2 0}, {2 0 0}, and {1 1 1} planes of the PdO phase.

We compared the NO_2 sensing properties of the fabricated sensors based on Pd-functionalized (i.e. 700 °C-annealed) In_2O_3 nanowires and bare In_2O_3 nanowires, respectively. Fig. 5a displays the current–voltage curves obtained at various NO_2 pressures in the range of 6.9×10^0–3.3×10^3 Pa for the sensors based on bare and Pd-functionalized In_2O_3 nanowires. As shown in Fig. 5a, both sensors show current–voltage linear relationships in the measured range of NO_2 pressures, clearly indicating that good ohmic contacts between the nanowires and the electrode layers were formed, regardless of Pd functionalization. The ohmic contact enables us to obtain more accurate sensing properties caused by the adsorption and desorption process of gas molecules on the surface of In_2O_3 nanowires, compared to the contact showing a rectifying behavior. Fig. 5b shows the log-log plots of the conductance as a function of NO_2 partial pressure. With the conductance exhibiting a strong dependency on the NO_2 pressure, we suggest that its relationship at a fixed temperature can be written as: $\sigma = AP_{NO_2}^{1/m}$, where σ is the electrical conductivity, A is the proportional coefficient, P_{NO_2} is the pressure of NO_2 in the vacuum chamber and m is the exponent revealing the conductivity mechanism. This behavior is similar to the corresponding relationship in regard to the O_2 sensing properties [41]. The values of $1/m$ were estimated to be $-1/0.41$ and $-1/0.29$ for the bare and the Pd-functionalized In_2O_3 nanowires, respectively. The negative values indicate that n-type conduction behavior operates in both the bare and the Pd-functionalized In_2O_3 nanowires during adsorption and desorption of NO_2. It is noteworthy that the slope of the Pd-functionalized In_2O_3 nanowires is much steeper than that of the bare In_2O_3 nanowires, strongly suggesting that Pd functionalization significantly facilitates the adsorption/desorption of NO_2 on the surface of In_2O_3 nanowires.

Fig. 6a compares the transient responses at an NO_2 concentration of 3 ppm, between the sensors fabricated from the bare and the Pd-functionalized In_2O_3 nanowires, respectively. The resistance of the sensors increases upon exposure to NO_2, whereas it decreases upon removal of NO_2. A significant change in the shape of the transient response has been introduced by Pd-functionalization. The response times, defined as the time to reach 90% of the final

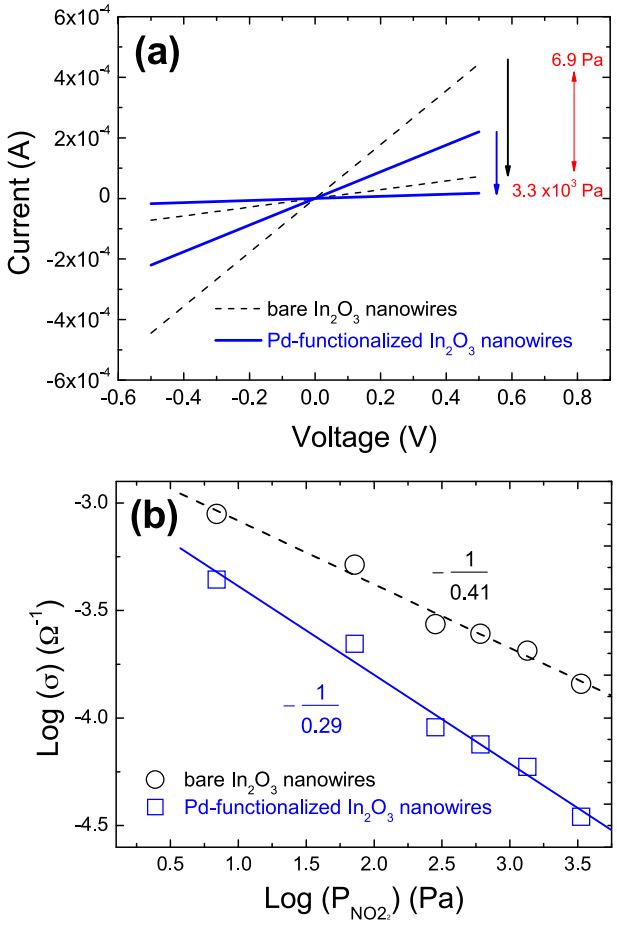

Fig. 5. (a) Current–voltage (I–V) curves obtained at various NO_2 pressures in the range of 6.9–3.3 × 10^3 Pa. (b) Log-log plots of conductance as a function of NO_2 partial pressure for sensors fabricated from bare and Pd-functionalized In_2O_3 nanowires.

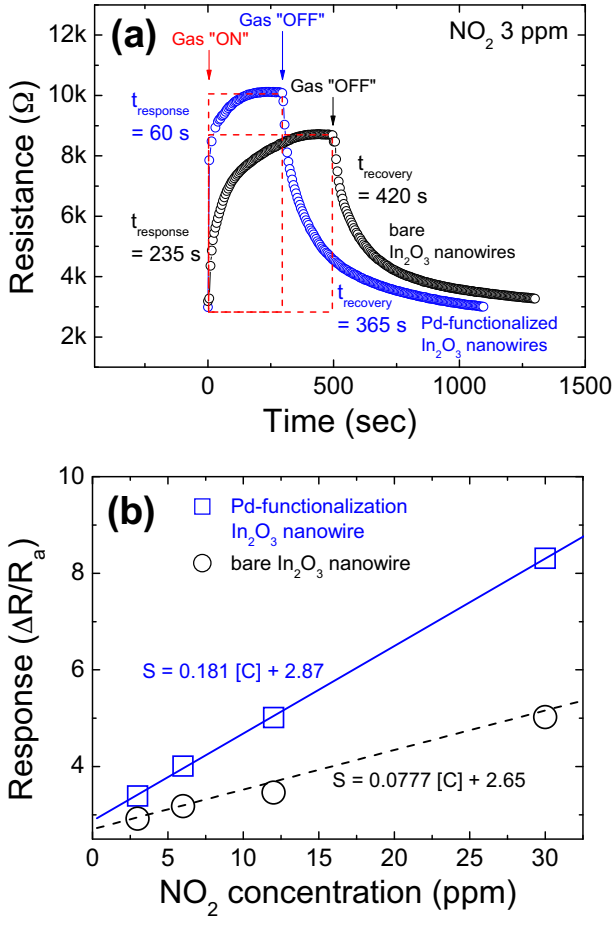

Fig. 6. (a) Dynamic responses at an NO_2 pressure of 3 ppm, for sensors fabricated from bare and Pd-functionalized In_2O_3 nanowires. (b) Sensitivity change with varying the NO_2 concentration, for sensors fabricated from bare and Pd-functionalized In_2O_3 nanowires.

value of resistance, of the sensors fabricated from the bare, and the Pd-functionalized In_2O_3 nanowires, are 60 and 235 s, respectively. By Pd-functionalization, the resistance increases more abruptly by exposing NO_2 gas, revealing that Pd-functionalization effectively quickens response time. The sensitivity (S) values were calculated according to the reported formula [21], $S = \Delta R/R = (R_g - R_0)/R_0$, where R_0 is the initial resistance in the absence of NO_2 and R_g is the resistance measured in the presence of NO_2. For both samples, the sensor response clearly tracks changes in the NO_2 environment, in which linear relationships were obtained between sensitivity and NO_2 concentration in the range of 0–30 ppm (Fig. 6b). The sensitivity of a semiconducting oxide is usually depicted as $S = A[C]^N + B$, where A and B are constants and [C] is the concentration of the target gas or vapor [42]. In the present study, the linear relationship reveals $N \approx 1.0$ for both samples. Most importantly, sensitivity was sharply enhanced by functionalizing the surface of In_2O_3 nanowires with Pd. Data fitting analyses revealed that $S = 0.181[C] + 2.87$ and $S = 0.0777[C] + 2.65$ for Pd-functionalized and the bare In_2O_3 nanowire sensors, respectively, suggesting that the enhancement of sensitivity becomes more evident at higher NO_2 concentrations.

The bundles of networked nanowires were deposited on the Si substrate and subsequently, the Pd shell layer was coated on the In_2O_3 core nanowires (Fig. 1b). For functionalization, the core–shell nanowires were thermally heated and thus the Pd/PdO shell layer was agglomerated to generate nanoparticle-like structures on the surface of the core nanowires (Supplementary material, S-4). Furthermore, the morphology of the agglomerated structure tended to change with varying the annealing temperature. The agglomeration of Pd can be attributed to the relatively high surface tension of Pd, in which Pd film is agglomerated to form Pd/PdO islands during thermal annealing. Diaz et al. reported that the Pd catalytic particles on SnO_2 nanopowders have been transformed to the PdO phase by thermal annealing at 800 °C [43]. Also, Shin et al. reported that the Pd/PdO nanoparticles were coalesced into larger PdO grains at the silica surface, by the annealing at 700 °C [44]. The formation mechanisms of PdO by thermal oxidation of Pd have been previously studied [45]. Although the annealing was carried out in Ar ambient, there exists the air leakage or the residual oxygen in the Ar flow, providing oxygen for the formation of PdO. The oxygen diffusion into the Pd surface is an initial step in the formation of PdO [46]. Although thin PdO films will form at low temperatures, the oxide growth will be retarded due to the formation of interfacial potential barrier blocks and thus the reduction of Pd ions movement. If thin films are exposed to an oxidizing atmosphere at elevated temperatures, thin PdO film will further grow, in which Pd ions acquire enough energy to drive the oxygen ionization.

Accordingly, we surmise that this technique can be applied to other core oxide nanowires sheathed with noble metals, with their generation and morphology being affected by properly adjusting the metal layer thickness and the thermal annealing process. Although the present sputtering technique needs to be developed to guarantee the uniform shell coating of core nanowires, other advanced techniques including chemical vapor deposition and atomic layer deposition can be applied.

Fig. 6b reveals that the NO_2 gas sensitivity has been enhanced by Pd functionalization. From the XRD (Fig. 2c) and TEM investigations, we surmise that the islands mainly consist of a mixture of Pd and PdO phases. Based on our literature survey, not only has the metal Pd been well known to promote spillover in a variety of gases, including H_2 [47], O_2 [48], and CO [49], but the PdO can also induce spillover of H_2 gas [50]. Accordingly, it is surmised that Pd/PdO can induce the spillover of other gases, including NO_2 gas.

We surmise that the NO_2 will react directly with surface indium ions [51], as it is similar to the case of SnO_2 surfaces. The adsorption of NO_2 to the substrate surface can be accomplished in different states, including NO_2^-, NO^+, and NO^- [52]. By the chemisorption reaction; $NO_2 + e^- \rightarrow NO_2^-$ [51,53], the resistance can be increased with the abstraction of electrons from the In_2O_3 surface. Furthermore, it is likely that the adsorbed NO_2 species (NO_2^-) are dissociated into NO(g) and O^-(ad), according to the reaction; $NO_2^- \rightarrow NO(g) + O^-(ad)$ [51]. While gaseous NO will easily evaporate, dissociated O^- facilitates the filling of oxygen vacancies by the following reactions: $2O^- + V_{O}^{\bullet\bullet} + e^- \leftrightarrow O^O$. Accordingly, these processes further help to increase the resistance of In_2O_3. On the other hand, the adsorbed NO_2 may be dissociated into nitrosyl forms (NO^+, NO^-). The O^- is supposed to be generated according to the reaction: $NO_2 \rightarrow NO^+ + O^-(ad)$, which thereby contributes to the increased resistance of In_2O_3. Also, oxygen adatoms may be produced during the generation of NO^-: $NO_2 + e^- \rightarrow NO^- + O(ad)$. The incorporation of oxygen adatoms can reduce oxygen vacancies ($V_{O}^{\bullet\bullet}$), with the formation of interfacial oxygen (O_O) and consequent reduction of electrons as follows: $O + V_{O}^{\bullet\bullet} + 2e^- \leftrightarrow O_O$, resulting in the increase of resistance [12]. Further detailed study is necessary in order to reveal the effect of oxygen adatoms on the sensing mechanisms.

We revealed that Pd-functionalization improved the NO_2-sensing characteristics of In_2O_3 nanowires (Supplementary material, S-4). The possible reasons for this will be discussed and suggested as follows. One possibility is that the Pd/PdO dispersed on the In_2O_3 surface will provide more active sites for NO_2 adsorption. In the case of Pd-functionalized In_2O_3 nanowires, the NO_2 is easily adsorbed on Pd/PdO particles and the adsorbed species can be migrated onto In_2O_3 core nanowire, which is less likely to be adsorbed by NO_2. S-4 describes the suppression of the conducting channel by Pd functionalization. Accordingly, by means of the NO_2-spillover effect, the adsorption of NO_2 species will be facilitated and thus the depletion layer can be enlarged, with the underlying conduction channel being suppressed. The reduction of conductance, which corresponds to the increase of the resistance, can be converted to intensification of the sensing signal, which corresponds to the enhancement of NO_2 sensitivity. Also, sufficient sensitivity can be attained even with a less amount of NO_2 gas, Pd-functionalization effectively will make the response time faster, agreeing with Fig. 6a.

Although further study is necessary, another possibility is that Pd/PdO facilitates the dissociation of NO_2 into ionized and/or non-ionized species, possibly including NO, O, NO_2^-, NO^+, and NO^-. For example, with NO_2 being a very efficient source of oxygen adatoms on the Pd surface [48], it is possible that NO_2 partially decomposes, producing adsorbed NO and oxygen adatoms ($NO_2 \rightarrow NO_a + O_a$) [54]. In the case of Pd-functionalized In_2O_3 nanowires, the NO_2 can be disassociated on Pd/PdO particles. Accordingly, by means of the spillover effect, the dissociated species will be transferred to In_2O_3 nanowires. Through the chemical reactions involving the dissociated species, resistance can be increased with the abstraction of electrons from the In_2O_3 surface. Accordingly, the reduction of conductance by the enlargement of the depletion layer, which corresponds to the increase of the resistance, can be converted to the intensification of the sensing signal in regard to the NO_2 gas.

4. Conclusions

We fabricated In_2O_3/Pd core–shell nanowires by means of a two-step process, in which Pd layers were sputtered onto the surface of networked In_2O_3 nanowires. Subsequently, the continuous Pd shell layers were transformed into crystalline islands by thermal heating. SEM images indicate that thermal annealing induced increased surface roughness and EDX investigation reveals that the roughness is associated with the agglomeration of the sputtered Pd shell. XRD and TEM investigations coincidentally reveal that the agglomerated islands on the nanowire surface mainly consist of a mixture of cubic Pd and cubic PdO phases. In the NO_2 gas sensing test, due to Pd-functionalization, the resistance increases more abruptly by exposing NO_2 gas, quickening the response time. Furthermore, the Pd-functionalized In_2O_3 nanowires exhibited exceptionally higher sensitivity than the bare nanowires and this tendency became more evident at higher NO_2 concentrations. The improvement of the sensing properties by Pd-functionalization is due not only to the enhanced adsorption or dissociation of NO_2, but also to the associated spillover effects.

Acknowledgements

This research was supported by Basic Science Research Program through the National Research Foundation of Korea (NRF) funded by the Ministry of Education, Science and Technology (2011-0009946).

Appendix A. Supplementary data

Supplementary data associated with this article can be found, in the online version, at doi:10.1016/j.jallcom.2011.06.104.

References

[1] D. Tsokkou, A. Othonos, M. Zervos, J. Appl. Phys. 106 (2009) 084307.
[2] S. Ishibashi, Y. Higuchi, Y. Nakamura, K. Oa, J. Vac. Sci. Technol. A 8 (1990) 1399–1402.
[3] S. Park, C. Jin, H.W. Kim, C. Lee, J. Alloys Compd. 509 (2011) 6262–6266.
[4] Y. Du, P. Ding, J. Alloys Compd. 507 (2010) 456–459.
[5] Z.M. Jarzebski, Phys. Status Solidi A71 (1982) 13–41.
[6] D.S. Ginley, C. Bright, Mater. Res. Soc. Bull. 25 (2000) 15–19.
[7] A.J. Miller, R.A. Hatton, G.Y. Chen, S. Ravi, P. Silva, Appl. Phys. Lett. 90 (2007) 023105.
[8] O.M. Berengue, A.J. Chiquito, L.P. Pozzi, A.J.C. Lanfredi, E.R. Leite, Nanotechnology 20 (2009) 245706.
[9] H.X. Liu, J. Sun, J. Jiang, Q.X. Tang, Q. Wan, IEEE Electron. Dev. Lett. 32 (2011) 313–317.
[10] H.X. Dong, S.L. Sun, L.X. Sun, W. Xie, L. Zhou, X.C. Shen, Z.H. Chen, Appl. Phys. Lett. 98 (2011) 011913.
[11] G.Z. Shen, J. Xu, X.F. Wang, H.T. Huang, D. Chen, Adv. Mater. 23 (2011).
[12] G. Neri, A. Bonavita, G. Licali, G. Rizzo, N. Pinna, M. Niederberger, Sens. Actuators B 127 (2007) 455–462.
[13] G. Korotcenkov, A. Cerneavschi, V. Brinzari, A. Vasiliev, M. MIvanov, A. Cornet, J. Morante, A. Cabot, J. Arbiol, Sens. Actuators B: Chem. 99 (2004) 297–303.
[14] M. Ivanovskaya, A. Gurlo, P. Bogdanov, Sens. Actuators B: Chem. 77 (2001) 264–267.
[15] M. Ali, C. Wang, C.C. Rohlig, V. Cimalla, T. Stauden, O. Ambacher, Sens. Actuators B: Chem. 129 (2008) 467–472.
[16] G. Korotcenkov, V. Brinzari, A. Cerneavschi, M. Ivanov, A. Cornet, J. Morante, A. Cabot, J. Arbiol, Sens. Actuators B: Chem. 98 (2004) 122–129.
[17] W.Y. Chung, G. Sakai, K. Shimanoe, N. Miura, D.D. Lee, N. Yamazoe, Sens. Actuators B: Chem. 46 (1998) 139–145.
[18] C. Ishibashi, T. Hyodo, Y. Shimizu, M. Egashira, Sens. Lett. 9 (2011) 369–373.
[19] J.Y. Liu, T. Luo, F.L. Meng, K. Qian, Y.T. Wan, J.H. Liu, J. Phys. Chem. C 114 (2010) 4887–4894.
[20] G. Leo, R. Rella, P. Siciliano, S. Capone, J.C. Alonso, V. Pankov, A. Ortiz, Sens. Actuators B 58 (1990) 370–374.
[21] S.T. Shishiyanu, T.S. Shishiyanu, O.I. Lupan, Sens. Actuators B 113 (2006) 468–476.
[22] C. Cantalini, W. Wlodarski, H.T. Sun, M.Z. Atashbar, M. Passacantando, A.R. Phani, S. Santucci, Thin Solid Films 350 (1999) 276–282.
[23] C. Cantalini, W. Wlodarski, H.T. Sun, M.Z. Atashbar, M. Passacantando, S. Santucci, Sens. Actuators B: Chem. 65 (2000) 101–104.

[24] P. Bogdanov, M. Ivanovskaya, E. Comini, G. Fagila, G. Sberveglieri, Sens. Actuators B: Chem. 57 (1999) 153–158.
[25] C.-Y. Lin, Y.-Y. Fang, C.-W. Lin, J.J. Tunney, K.-C. Ho, Sens. Actuators B 146 (2010) 28–34.
[26] W. Lim, J.S. Wright, B.P. Gila, J.L. Johnson, A. Ural, T. Anderson, F. Ren, S.J. Pearson, Appl. Phys. Lett. 93 (2008) 072109.
[27] J.W. Lee, D. Jang, G.T. Kim, M. Mouis, G. Ghibaudo, J. Appl. Phys. 107 (2010) 044501.
[28] M. Law, H. Kind, B.B. Messer, F. Kim, P.D. Yang, Angew. Chem. Int. Ed. 41 (2002) 2405–2408.
[29] E. Comini, G. Faglia, G. Sberveglieri, Z.W. Pan, Z.L. Wang, Appl. Phys. Lett. 81 (2002) 1869–1871.
[30] P. Xu, Z. Cheng, Q. Pan, J. Xu, Q. Xiang, W. Yu, Y. Chu, Sens. Actuators B 130 (2008) 802–808.
[31] G. Shen, Recent Patents Nanotechnol. 2 (2008) 160–168.
[32] J. Huang, Q. Wan, Sensors 9 (2009) 9903–9924.
[33] L. Liu, T. Zhang, S. Li, L. Wang, Y. Tian, Mater. Lett. 63 (2009) 1975–1977.
[34] V.D. Kapse, S.A. Ghosh, F.C. Raghuwanshi, S.D. Kapse, Sens. Actuators B 137 (2009) 681–686.
[35] Y.D. Zhang, Z. Zheng, F.L. Yang, Ind. Eng. Chem. Res. 49 (2010) 3539–3543.
[36] S.W. Choi, J.Y. Park, S.S. Kim, Nanotechnology 20 (2009) 465603–465608.
[37] Y. Park, S.W. Choi, J.W. Lee, C. Lee, S.S. Kim, J. Am. Ceram. Soc. 92 (2009) 2551–2554.
[38] H.W. Kim, S.H. Shim, J.W. Lee, J.Y. Park, S.S. Kim, Chem. Phys. Lett. 456 (2008) 193–197.
[39] J.Y. Park, S.W. Choi, S.S. Kim, Nanoscale Res. Lett. 5 (2010) 353–359.
[40] T.R. Thomas, Rough Surfaces , 2nd ed., Imperial College Press, London, 1999.
[41] Y. Xu, X. Zhou, O.T. Sorenson, Sens. Actuators B: Chem. 65 (2000) 2–4.
[42] Q. Wan, J. Huang, Z. Xie, T. Wang, E.N. Dattoli, W. Lu, Appl. Phys. Lett. 92 (2008) 102101.
[43] R. Diaz, J. Arbiol, A. Cirera, F. Sanz, F. Peiro, A. Cornet, J.R. Morante, Chem. Mater. 13 (2001) 4362–4366.
[44] J. Shin, T.-L. Ha, I.S. Lee, Eur. J. Inorg. Chem. 2010 (2010) 357–360.
[45] O. Garcia-Serrano, C. Lopez-Rodriguez, J.A. Andraca-Adame, G. Romero-Paredes, R. Pena-Sierra, Mater. Sci. Eng. B 174 (2010) 273–278.
[46] H.H. Kan, J.F. Weaver, Surf. Sci. 603 (2009) 2671–2682.
[47] A.J. Du, S.C. Smith, X.D. Yao, G.Q. Lu, J. Am. Chem. Soc. 129 (2007) 10201–10204.
[48] B.A. Banse, B.E. Koel, Surf. Sci. 232 (1990) 275–285.
[49] M. Eriksson, L.G. Petersson, Surf. Sci. 311 (1994) 139–152.
[50] L.F. Chen, J.A. Wang, M.A. Valenzuela, X. Bokhimi, D.R. Acosta, O. Novaro, J. Alloys Compd. 417 (2006) 220–223.
[51] B. Ruhland, Th. Becker, G. Müller, Sens. Actuators B 50 (1998) 85–94.
[52] J. Tamaki, M. Nagaishi, Y. Teraoka, N. Miura, N. Yamazoe, Surf. Sci. 221 (1989) 183–196.
[53] S.H. Wang, T.C. Chou, C.C. Liu, Sens. Actuators B 94 (2003) 343–351.
[54] T. Jirsak, J. Dvorak, J.A. Rodriguez, Surf. Sci. 436 (1999) L6683.